

1 **An efficient approach for inverting rock exhumation from thermochronologic age-elevation**
2 **relationship**

3

4 Yuntao Tian^{1,2*}, Lili Pan¹, Guihong Zhang¹, Xinbo Yao¹

5

6 ¹ Guangdong Provincial Key Laboratory of Geodynamics and Geohazards, School of Earth
7 Sciences and Engineering, Sun Yat-sen University, Guangzhou 510275, China

8 ² Southern Marine Science and Engineering Guangdong Laboratory (Zhuhai), Zhuhai 519082,
9 China

10

11 *Corresponding author:

12 Yuntao Tian

13 tianyuntao@mail.sysu.edu.cn

14

15

16 **Abstract**

17 This study implements the least-squares inversion method for solving the exhumation history from
18 thermochronologic age-elevation relationship (AER) based on the linear equation among
19 exhumation rate, age and total exhumation from the closure depth to the Earth surface. Modelling
20 experiments suggest significant and systematic influence of initial geothermal model, the *a priori*
21 exhumation rate and the time interval length on the *a posteriori* exhumation history. Lessons
22 learned from the experiments include that (i) the modern geothermal gradient can be used for
23 constraining the initial geothermal model, (ii) a relatively higher *a priori* exhumation rate would
24 lead to systematically lower *a posteriori* exhumation, and *vice versa*, (iii) the variance of the *a*
25 *priori* exhumation rate controls the variation of the inverted exhumation history, (iv) the choice of
26 time interval length should be optimized for resolving the potential temporal changes in
27 exhumation. To mitigate the dependence of inverted erosion history on these initial parameters,
28 we implemented a new stepwise inverse modeling method for optimizing the model parameters
29 by comparing the observed and predicted thermochronologic data and modern geothermal
30 gradients. Finally, method demonstration was performed using four synthetic datasets and three
31 natural examples of different exhumation rates and histories, It is shown that the inverted rock
32 exhumation histories from the synthetic datasets match the whole picture of the “truth”, although
33 the temporal changes in the magnitude exhumation are underestimated. Modelling of the datasets
34 from natural samples produce geologically reasonable exhumation histories. The code and data
35 used in this work is available in GitHub (https://github.com/yuntao-github/A2E_app).

36
37 **Key words:** Thermochronology; Exhumation; Numerical inversion; Age-elevation relationship;
38 Least-squares method; Geothermal model

Deleted: thermochronologic

Deleted: demonstrate the

Deleted: inversion results

Formatted: Font: Italic

Deleted: Putting together these findings,

Deleted: propose

Deleted: strategy

Deleted: to mitigate the model dependencies on the initial parameters

Deleted: we use

Deleted: for method demonstration

Deleted: It is shown that

Deleted: our new modelling strategy

Deleted: s

Deleted: and geothermal gradients that are consistent with both the observed AER and modern geothermal data

Deleted: <https://github.com/yuntao-github/code4modelAER>

55 **1. Introduction**

56 Quantifying rock exhumation from the Earth interior to the surface is important information for
57 better understanding many geological problems, ranging from orogenic growth (e.g., Zeitler et al.,
58 2001; Whipp Jr. et al., 2007) and decay (e.g., House et al., 2001; Hu et al., 2006), to resource and
59 hydrocarbon evaluation and exploration (e.g., Armstrong, 2005; McInnes et al., 2005), as well as
60 the underpinning endogenic and exogenic processes and their interactions (e.g., Burbank et al.,
61 2003; Fox et al., 2015; Tian et al., 2015). Various experimental and modeling methods have been
62 invented for estimating the rock exhumation at different crustal levels (e.g., Braun, 2003; Reiners
63 and Brandon, 2006; Anderson et al., 2008; Braun et al., 2012; Fox et al., 2014).

64 One type of the methods for estimating the rock exhumation in the middle and upper crust
65 relies on thermochronologic cooling ages acquired from by noble gas and fission-track dating of a
66 series of accessory minerals, such as Ar-Ar, fission-track and (U-Th)/He analyses (Ault et al., 2019
67 and references therein). Based on the closure temperature theory (Dodson, 1973), assuming
68 monotonic cooling, a thermochronologic age records the time duration that a rock cooled through
69 the corresponding closure temperature, which is a function of the kinematics describing fission-
70 track annealing and noble gas diffusion, and rock cooling rate (Dodson, 1973). If the depth of the
71 closure temperature isotherm can be estimated from the crustal temperature field, a time-averaged
72 exhumation rate can be obtained from the cooling age.

73 Based on the thermochronologic methods and thermo-exhumation modelling, many
74 analytical and numerical tools have been implemented for inverting the exhumation and/or the
75 associated cooling history from thermochronologic data. These tools have different functions, such
76 as inverting temperature history (Laslett et al., 1987; Ketcham, 2005; Gallagher, 2012),
77 determining time-averaged exhumation rates (Brandon et al., 1998; Ehlers, 2005; Willett and

Deleted: Rock

Deleted: mountain building

Deleted: its

Deleted: ,

Deleted: mica

Deleted: apatite, zircon and titanite

Deleted: (Farley, 2002; Reiners, 2005)

Deleted: cooling

86 Brandon, 2013; Glotzbach et al., 2015; Van Der Beek and Schildgen, 2023), spatiotemporal
87 changes in exhumation (Sutherland et al., 2009; Herman et al., 2013; Fox et al., 2014; Willett et
88 al., 2020), and evolution of exhumation in two or three dimensions given a tectonic framework
89 (Batt and Brandon, 2002; Braun, 2003; Van Der Beek et al., 2010; Valla et al., 2011; Braun et al.,
90 2012).

91 Convincing estimate of exhumation history for a region requires both a proper sampling
92 strategy for thermochronologic data and a robust modeling approach for exhumation inversion,
93 especially when the rock exhumation and its spatiotemporal changes are tectonically controlled
94 (Ehlers and Farley, 2003; Schildgen et al., 2018). A routine and efficient sampling strategy
95 acquires thermochronologic ages from an elevation transect over a significant relief and a relatively
96 confined spatial distance. Plotting the age versus elevation, i.e., the age-elevation relationship
97 (AER), and analyzing the slope changes of the plot can provide first-order understanding of the
98 exhumation history (Fitzgerald et al., 1986). Because both the subsurface geothermal field and
99 closure temperature of thermochronometers are functions of the thermal advection and cooling
100 during rock exhumation (e.g., Dodson, 1973; Brandon et al., 1998), as well as the long-wavelength
101 topography (Braun, 2002; Ehlers and Farley, 2003; Glotzbach et al., 2015), Estimating reliable
102 exhumation rates requires to account for temporal variations of the thermal field caused by changes
103 in the thermal and kinematic boundary conditions,

104 Fox et al. (2014) reported a linear inversion modeling method that solves exhumation
105 history from AER, given a combination of *a priori* exhumation rates and assumed geothermal
106 parameters. However, as shown in that study, the inverted exhumation history depends highly on
107 these *a priori* values and geothermal assumptions. Building on that study, we here provide a

Deleted: underground

Deleted: reliable estimates of exhumation rates require solving exhumation itself, together with the evolution of other influencing factors

112 detailed test on the method and report an improved modeling method that makes use of both the
113 AER and the modern geothermal gradient for inverting exhumation history. ▽

Deleted: strategy

Deleted: Other suggestions for model setup are also provided in this work.

115 2. Linear inversion method

116 Our inversion of exhumation from thermochronologic data followed the linear inversion
117 approach of Fox et al. (2014). Rock Exhumation from the closure depth of a thermochronometer,
118 z_c , to the Earth's surface can be described as an integral of the exhumation ($\dot{\epsilon}$) from the cooling
119 age (τ) to the present (Brandon et al., 1998; Fox et al., 2014). For a set of correlated bedrock
120 samples with a shared history of exhumation rates ($\dot{\epsilon}$), their thermochronologic ages (\mathbf{A}) and the
121 corresponding closure depths (\mathbf{z}_c) can be expressed by the following equation.

$$122 \int_0^{\tau} \dot{\epsilon} dt = z_c \Rightarrow \mathbf{A}\dot{\epsilon} = \mathbf{z}_c, \quad (1)$$

123 where \mathbf{A} is a model matrix, with n rows (the total number of samples) and m columns (the total
124 number of time intervals). Each row of the matrix is a discretization of a sample age, which is
125 composed of a number of time lengths (Δt) followed by an age residual (R_i) and a number of zeros.
126 The $\dot{\epsilon}$ is a m -length vector of exhumation rates, and the \mathbf{z}_c is n -length vector of closure depths.

127 This linear equation can be solved using the Least-Squares Regression approach assuming
128 the Gaussian uncertainties and *a priori* mean exhumation rate ($\dot{\epsilon}_{pr}$) and associated variance (σ_{pr})
129 (Tarantola, 2005; Fox et al., 2014). Such an approach requires a $m \times m$ -sized parameter covariance
130 matrix, \mathbf{C} , and a $n \times n$ -sized data covariance matrix, \mathbf{C}_g , which includes the uncertainties on the
131 closure depths. These two matrices can be constructed as equations 2 and 3, respectively.

$$132 C_{ij} = \begin{cases} \sigma_{pr}^2, & \text{if } i = j \\ 0, & \text{if } i \neq j \end{cases} \quad (2)$$

$$133 (C_g)_{ij} = \begin{cases} \dot{\epsilon}_{pr} \epsilon_i, & \text{if } i = j \\ 0, & \text{if } i \neq j \end{cases}, \quad (3)$$

137 where \hat{e}_{pr} and σ_{pr} are the *a priori* exhumation and the associated variance, and the ε_i is analytical
 138 uncertainty of the age data. The construction of the data covariance matrix assumes the age data
 139 are uncorrelated. Worth noting is that previous studies used different constructions of the data
 140 covariance, changing from using the analytical age uncertainties (Fox et al., 2014; Fox et al., 2015)
 141 to constant values (Jiao et al., 2017; Stalder et al., 2020).

142 Given the above model parameters, the equation 1 has a maximum likelihood solution for
 143 the exhumation rate vector:

$$144 \quad \hat{e}_{po} = \hat{e}_{pr} + \mathbf{CA}^T(\mathbf{ACA}^T + \mathbf{C}_\epsilon)^{-1}(\mathbf{z}_c - \mathbf{A}\hat{e}_{pr}), \quad (4)$$

145 where \hat{e}_{pr} is a n-length vector of \hat{e}_{pr} , \mathbf{z}_c is the n-length vector of closure depths calculated using a
 146 combination of exhumation and geothermal model parameters (see section 3). The \hat{e}_{po} is the
 147 posteriori maximum likelihood estimate of the exhumation rate, with a covariance matrix, \mathbf{C}_{po} ,
 148 which provides an estimate of the uncertainties on the model parameters (equation 5).

$$149 \quad \mathbf{C}_{po} = \mathbf{C} - \mathbf{CA}^T(\mathbf{ACA}^T + \mathbf{C}_\epsilon)^{-1}\mathbf{AC} \quad (5)$$

150 The method also provides a model resolution matrix, \mathbf{R} , which gives a measure on how
 151 well the model estimates correspond to the true values:

$$152 \quad \mathbf{R} = \mathbf{CA}^T(\mathbf{ACA}^T + \mathbf{C}_\epsilon)^{-1}\mathbf{A}. \quad (6)$$

154 3. Closure depth and topographic correction

155 Inversion of the exhumation using the equation 1 requires accurate estimates of the closure
 156 depths of the thermochronologic ages (\mathbf{z}_c), i.e., the depth of the closure temperatures (Fig. 1). The
 157 latter can be determined by modelling the temperature of the crust using a 1D thermal-kinematic
 158 model, which accounts for heat conduction, advection and production, (Turcotte and Schubert,
 159 2002):

Deleted: These depths can be determined from the underground temperature model, which can be simplified as and calculated by the following 1D thermal conduction and convection equation

$$\frac{\partial T_m}{\partial t} = \kappa \frac{\partial^2 T_m}{\partial z^2} + \dot{e} \frac{\partial T_m}{\partial z} + A_b, \quad (7)$$

where A_b is the heat production (in °C/Myr). This function can be numerically solved using a Crank–Nicolson time integration with a set of initial and boundary conditions, such as an initial geothermal gradient (G0) at the start time of the model and surface temperature (T_s) (Turcotte and Schubert, 2002; Fox et al., 2014).

The closure temperature (T_c) of a thermochronometer is a function of cooling rate (\dot{T}) at the closure time and kinetic parameters of Helium and Argon diffusion and fission-track annealing in mineral phases (Dodson, 1973):

$$\dot{T} = \frac{\Omega R T_c^2}{E_a} \exp\left(\frac{-E_a}{R T_c}\right), \quad (8)$$

where Ω and E_a are the diffusion frequency factor normalized by the mineral size and geometry, and activation energy, respectively. Parameter R is the gas law constant. See reviews by Reiners and Brandon (2006) for the Ω and E_a parameter values for different thermochronometers.

The cooling rate (\dot{T}) can be computed from the derivative of transient geotherms, $T_m(t, z)$ that can be computed using equation 7 (Fox et al., 2014):

$$\dot{T} = \frac{\partial T_m}{\partial t} + \dot{e} \frac{\partial T_m}{\partial z}, \quad (9)$$

where \dot{e} is unknown exhumation that can be computed through the equation 1.

Combining the equations 7-9, the closure depth of a thermochronological system ($z_{c,m}$) can be numerically computed. This depth also needs a topographic correction, because of the topographic perturbation, p , on the isotherms (Braun, 2002; Ehlers and Farley, 2003; Fox et al., 2014; Glotzbach et al., 2015). Such a perturbation can be determined by the following equation (Mancktelow and Grasemann, 1997; Fox et al., 2014):

$$p(\lambda) = \left(\frac{y_0 - y_a}{y_{zm}}\right) \exp\left(-z_m \left(\frac{\dot{e}}{2\kappa} + \sqrt{\left(\frac{\dot{e}}{2\kappa}\right)^2 + (2\pi\kappa)^2}\right) h(\lambda)\right), \quad (10)$$

186 where γ_a is the atmospheric lapse rate, γ_0 and γ_{z_m} are the thermal gradients at the model surface and
 187 at the depth z_m . The $h(\lambda)$ is a cosine function expression of the model surface topography, which
 188 can be determined using the discrete Fast Fourier Transform at the frequency domain. Here we use
 189 the SRTM30 data for computing the topography of regions of interests.

190 Finally, the closure depth of the z_c is corrected by the topographic perturbation (e.g.,
 191 Brandon et al., 1998):

$$(z_c)_i = (z_{c,m})_i - p_i + h_i, \quad (11)$$

192 where $z_{c,m}$ is the closure depth calculated using the 1D geothermal model, p and h are the
 193 topographic perturbation and elevation difference with respect to the mean elevation at the sample
 194 site (Fig. 1), and the i denotes the i -th age.

196 As shown by the equations 7, 8 and 9, the closure depth is a non-linear function of rock
 197 cooling and exhumation. Therefore, the problem of interest is non-linear, which can be addressed
 198 by iterative numerical modelling methods. In this work, the solution of exhumation is
 199 approximated by coupling and iterating the linear inversion and closure depth modeling. As shown
 200 in Tarantola (2005) and Fox et al. (2014), the algorithm converges in a few iterations and produces
 201 stable outputs.

203 4. Model evaluation

204 Quantitative model assessment relies on a misfit value, i.e., the difference between
 205 observed and predicted ages weighted by the observed analytical uncertainty;

$$\Phi_\tau = \sqrt{\frac{1}{N} \sum_{i=1}^N \left(\frac{\tau_{prd,i} - \tau_{obs,i}}{\varepsilon_i} \right)^2}, \quad (12)$$

207 where $\tau_{obs,i}$ and $\tau_{prd,i}$ are the observed and predicted i -th age calculated from the exhumation history,
 208 and ε_i is the uncertainty of the observed i -th age. Following Fox et al. (2014), both the *a priori* and

Deleted: the

Deleted: fitness of the predicted ages to the observed, using the following misfit function

212 *a posteriori* misfits, $\Phi_{\tau, pr}$ and $\Phi_{\tau, po}$, are determined for the models. The difference between these
213 two misfit values provides a measure of the model improvements. A smaller posteriori misfit value
214 indicates an improved model result, and *vice versa*.

Deleted: data fitness

215 To evaluate the geothermal parameters, we also determined the misfit value of the
216 predicted to the observed modern geothermal gradient value using the following equation:

$$217 \quad \Phi_{\gamma} = \sqrt{\left(\frac{\gamma_{prd} - \gamma_{obs}}{\varepsilon_{\gamma}}\right)^2}, \quad (13)$$

218 where γ_{prd} and γ_{obs} are the predicted and observed geothermal gradients, and ε_{γ} is the uncertainty
219 of the observed value. Because the depth-temperature curves are slightly non-linear, the predicted
220 geothermal gradient (γ_{prd}) is calculated as a mean value for the upper 1 km of the model. Similar
221 as the assessment of age data, we also determined the *a priori* and *a posteriori* misfits, $\Phi_{\gamma, pr}$ and
222 $\Phi_{\gamma, po}$ values for assessing the geothermal parameters.

223

224 5. The reference inverse model

225 Following Willett and Brandon (2013) and Fox et al. (2014), here we use the published
226 AFT data acquired from Denali Massif (Fitzgerald et al., 1995) for method demonstration (Fig.
227 2a). A break-in-slope is shown by the AER at ~ 7 -6 Ma, indicating a coeval change in slope, i.e.,
228 the apparent exhumation rate (Fitzgerald et al., 1995), increasing from 0.17 ± 0.04 km/Myr to 1.2
229 ± 0.6 km/Myr (Fig. 2b). AER regression of young dates from the lower part of the transect
230 (between 4.3-2.0 km) also predicts a closure depth that is the intercept at -3.3 ± 3.4 km (Fig. 2b).
231 However, using the present geothermal gradient (38.9 °C/km) (Fox et al., 2014) and a nominal
232 closure temperature of AFT method (110 °C) (Reiners and Brandon, 2006) and a -12 °C surface
233 temperature (Fox et al., 2014), the closure depth is predicted as ~ 3.1 km beneath the mean elevation

Deleted: change

236 (~4 km), which is equivalent to an elevation of ~0.9 km. This closure depth is significantly higher
237 than the intercept (-3.3 ± 3.4 km). Such a difference indicates the AER slope of the lower part
238 overestimates the exhumation rates since ~7-6 Ma.

239 Following the protocol outlined in Fox et al. (2014), the reference inverse model uses the
240 following parameters, a start time at 25 Ma, a time interval (Δt) of 2.5 Myr, a 4020 m mean
241 elevation, a -12 °C surface temperature, *a priori* exhumation rate of 0.5 ± 0.15 km/Myr, a 24 °C/km
242 initial geothermal gradient, a 38.9 °C/km present geothermal gradient, a model block with a
243 thickness of 80 km, and a 30 km²/Myr thermal diffusivity.

244 The exhumation history output of the reference model is shown in Fig. 3. The inversion
245 results reveal an more than two-fold increase of exhumation rate to a value of ~0.6 km/Myr at 7.5
246 Ma (Fig. 3b), consistent with the development of the break-in-slope in the AER. The model also
247 shows a gradual decrease of exhumation rate from *a priori* exhumation rate (0.5 km/Myr) to 0.3
248 km/Myr from 25 Ma to 7.5 Ma. The invariant exhumation during the starting stage resulted from
249 the fact that all ages are younger than 17.5 Ma, and thus the data have no resolution for the time
250 span. These results are similar to those of Fox et al. (2014). The posteriori misfit for the age is
251 1.88, significantly smaller than that of the priori model (4.51), suggesting the improvement by the
252 inverse modeling (Fig. 3b). Such a model also provides reasonable fit to the modern temperature
253 field, as shown by the small misfit (0.39) in the geothermal gradient (Fig. 3b).

254 The resolution of the inverted exhumation history can be assessed by the resolution matrix
255 **R** (equation 6). Imaging of the matrix shows the model provides no resolution for the time period
256 before 17.5 Ma (Fig. 3c), consistent with the fact that the oldest input age is younger than $16.1 \pm$
257 0.9 Ma. For the time span between 15 and 5 Ma, the model resolution is high, as shown by the
258 diagonal elements of the matrix, with the highest resolution at 7.5-5 Ma span, including eight age

Deleted: Same as used in

Deleted: abrupt

Deleted: triple

Deleted: -four

Deleted: 55-0.7

Deleted: 7.5

Deleted: 15

Deleted: 10

Deleted: 73

Deleted: 68

Deleted: 01

Deleted: youngest

271 date points (Fig. 3c). The most recent two phases of exhumation (5-0 Ma) are less resolved, as
272 shown by the nearly equal resolution values for the two phases, i.e., the latest four pixels of the
273 matrix (Fig. 3c). ~~This is because no input ages fall into this time span, when the~~ modeled
274 exhumation results are time-averaged values. The slight decrease in the last stage reflects changes
275 in geothermal gradient.

Deleted: , as no ages fall into this time interval

Deleted: The

Deleted: for the time interval

Deleted: thus

276 For assessing the correlation among model parameters, the calculated covariance matrix is
277 scaled by the diagonal covariance matrix (Fox et al., 2014):

$$278 \hat{C}_{\xi\beta} = \frac{C_{\xi\beta}}{\sqrt{C_{\xi\xi}}\sqrt{C_{\beta\beta}}}. \quad (14)$$

279 The correlation matrix for the reference model is shown in Fig. 3d. The diagonal correlation
280 values are 1 and off-diagonal ones are dominantly negative, indicating anti-correlated uncertainties
281 (Fig. 3d), which suggests exhumation parameters were not resolved independently by the modeling.
282 In fact, it is expected to have the anti-correlation, because, given two steps of rock exhumation,
283 decreasing the exhumation during one step would increase that of the other step.

284

285 6. Dependence on model parameters and proposed solutions

286 Here we use the Denali data set for demonstrating the influences of (1) the initial
287 geothermal parameters, (2 and 3) the *a priori* mean and variance values of the exhumation rates,
288 and (4) time interval length on the inverted exhumation history. Also discussed in this section are
289 the solutions for optimizing the model setup for these parameters.

290

291 6.1. Dependence on initial thermal model

292 Different initial model geothermal parameters would lead isotherms to shift either
293 downward to greater depths or upwards to the Earth surface, and either compression or expansion

298 among isotherms. Therefore, the initial thermal models have systematic influence on the closure
299 depths and consequently the *a posteriori* exhumation.

300 This is demonstrated by modelling experiments presented in Figure 4. Using a relatively
301 lower initial geothermal gradient produces relatively higher *a posteriori* exhumation rates
302 (comparing the models shown in Figs. 4a-4f), and *vice versa*. Such an influence is significant even
303 for the time and elevation intervals with multiple age constraints (10-5.0 Ma). For example, using
304 relatively lower geothermal gradients of <22 °C/km would yield significantly higher average
305 exhumation rates of >0.75 km/Myr for the last two stages (<5 Ma) (Figs. 4a-4c) than those (<0.6
306 km/Myr) using higher initial geothermal gradients of ≥ 26 °C/km (Figs. 4d-f). Further, it is also
307 shown that models using higher and lower prior geothermal gradients of <20 °C/km (Figs. 4a-4b)
308 and >30 °C/km (Figs. 4e-4f) yield worse misfits ($\Phi_{\chi, po} > 1$) for the observed present-day
309 geothermal gradient than those ($\Phi_{\chi, po} < 1$) using medium initial gradients (22-26 °C/km) (Figs. 3
310 and 4c-4d).

Deleted: 8

Deleted: Worth noting is that the models using relatively lower (16-20 °C/km, Figs. 4a-4b) and higher (30-34 °C/km, Figs. 4e-4f) initial geothermal gradients yield relatively worse misfits (>1) than those using medium initial gradients (22-26 °C/km) (Figs. 3 and 4c-4d), suggesting that the modern geothermal gradient can be used as a constraint for the initial geothermal model.

311 These results highlight the importance of taking geothermal parameters into account in
312 inverting the exhumation history and model evaluation. We proposed to run a set of models using
313 different *a priori* geothermal parameters, especially the initial geothermal gradient, to search for
314 the proper initial geothermal setup that provides reasonable fits to both the ages and the modern
315 geothermal gradient (see section 7 for details).

316

317 6.2. Dependence on the *a priori* exhumation rate

318 Both the mean and variance of the *a priori* exhumation rate have important influences on
319 the model solution for the maximum likelihood estimation method. Our modeling experiments
320 show that the mean value of the *a priori* exhumation has systematic influences on the inverted

329 exhumation. Similar to the reference model, exhumation of the preceding three stages (25-17.5
330 Ma) without age constraints is the same as the *a priori* input. For the following stages, a relatively
331 higher mean value of the *a priori* exhumation results in relatively lower *a posteriori* exhumation
332 rates (comparing different models presented in Fig. 5). For example, models using the mean *a*
333 *priori* exhumation of ≤ 0.4 km/Myr yield a *posterior* exhumation of 0.5-0.9 km/Myr for the stages
334 < 7.5 Ma (Figs. 5a-5c), whereas those using a higher *a priori* value (≥ 0.6 km/Myr) result in a
335 *posterior* exhumation of 0.45-0.6 km/Myr for the same stages (Figs. 5d-5f). This is because a
336 relatively higher *a priori* value, which would be used for calculating thermal models, would lead
337 to a quicker increase in geothermal gradient and thus relatively shallower closure depths and
338 relatively lower exhumation rates.

339 The variance of the *a priori* exhumation rate has important influence on both the
340 exhumation rates and the posterior variance. Models with lower *a priori* variances yield less
341 variations in the *a posteriori* exhumation history, and *vice versa* (comparing models in Fig. 6).
342 Further, models using the input variance of the *a priori* exhumation of 0.2-0.3 km/Myr (40-60%
343 of the mean value), the variation of the inverted exhumation history becomes stable (Figs. 3, 6c-
344 6d). Given that the uncertainty of the input age data, which is often 10%-20% at a two-sigma level,
345 larger variance of the inverted exhumation would be unreasonable (Figs. 6e-6f), especially when
346 multiple age data are available at different elevations.

347 We proposed to run a set of models using different *a priori* mean value of erosion rates to
348 search for the one that provides appropriate fits to both the ages and the modern geothermal
349 gradient. As to the *a priori* variance, we propose to use a value 30-70% of the *a priori* erosion rate.
350 Future applications of the method may need to test a set of the variance inputs so as to get a stable

Deleted: 5

Deleted: 8

Deleted: 7

Deleted: of erosion rates

Deleted: relative uncertainty

Deleted: of

Deleted: mean value

358 exhumation output. Larger *a priori* variance would lead to larger uncertainties for the exhumation
359 rates, which is unreasonable and non-meaning for geological studies.

361 6.3. Dependence on time interval length

362 Constraining the onset time of major changes in exhumation rates is one of the important
363 tasks for inverting the exhumation history from thermochronologic data. Using a large time
364 interval length cannot accurately capture the potential transition time of exhumation rates. As
365 shown in the Figs. 7b-7d, models using time lengths of ≤ 3.5 Ma show an abrupt increase in
366 exhumation at 7-6 Ma, consistent with that shown in AER plot. However, the models using a large
367 time interval length (≥ 4.5 Ma) overestimate the onset time of the enhanced exhumation (Figs. 7e-
368 7f). Further, a relatively shorter time length would smooth temporal changes in exhumation rates,
369 leading to an underestimating of the variations. For example, as shown in the Fig. 7a, the model
370 using a relatively shorter time length (0.5 Ma) yields an exhumation variation between 0.35-0.60
371 km/Myr, significantly lower than those using relatively larger time interval lengths (Figs. 7b-7f).
372 In addition, a shorter time length also significantly increases the computational time and resources,
373 especially when processing a large number of vertical transects.

374 Given the interests in major exhumation changes, we propose the time interval length (Δt)
375 should be optimized for constraining the transitional time and the associated exhumation changes.
376 Therefore, the time interval length should be set as the absolute uncertainty at two sigma levels at
377 the break point (τ_b) (equation 15). If the break point is unclear in AER, we suggest to use the
378 absolute uncertainty at two-three sigma levels at the median age value ($\tilde{\tau}$) (equation 15), so as to
379 focus on the time intervals where ages cluster.

$$380 \quad \Delta\tau = \begin{cases} \delta\tau_b, & \text{if a break in slope exists} \\ \delta\tilde{\tau}, & \text{if no clear break in AER} \end{cases}, \quad (15)$$

Deleted: propose

382 where δ is the relative age uncertainty at two sigma levels, varying between 10%-20% among
383 different studies. Following this method, the Denali case should use a time length of ~1.5 Ma (7
384 Ma \times 20%), slightly lower than that used in the reference model (Fig. 3).

385

386 7. A new modeling guideline,

387 Following the modelling protocol outlined above, a stepwise modeling guideline is
388 developed for addressing the model dependencies on the initial geothermal parameter, the *a priori*
389 exhumation rates and time interval length. As illustrated in the Figure 8, the approach includes the
390 following three steps.

391 (i) Estimating a time-averaged erosion rate. Dividing each nominal closure depth, which
392 can be estimated from the nominal closure temperatures and the modern geothermal gradient, by
393 the corresponding age results in a time-averaged erosion rate. Then, a mean value can be
394 determined by averaging the rates. Such a mean value and assumed variance (30% - 50% in this
395 work) will be used as the *a priori* erosion rate.

396 (ii) Optimizing the fit to the modern geothermal gradient. This step runs a set of inversion
397 models (20 in this work) using different geothermal gradients, ranging from 50% to 120% of the
398 modern value, together with the *a priori* erosion rate estimated in the first step, for determining
399 the initial geothermal gradient that yields the maximum fit to the modern value, i.e., the minimum
400 Φ_γ (equation 13).

401 (iii) Optimizing the fit to both the age data and the geothermal gradient. Given the model
402 dependence on the geothermal parameters (see section 6.1), a comprehensive evaluation of the
403 models should assess not only the age misfit (Φ_τ), but also that of the geothermal gradient (Φ_γ). In
404 the third step, a set of inversion models (20 in this work) are run using different *a priori* erosion

Deleted: strategy

Deleted: Putting together the lessons learned from the above modelling experiments

Deleted: new

Deleted: strategy

Deleted: develops

Deleted: 60

412 rates, changing from 10% to 200% of the mean value estimated in the first step, together with the
413 estimated geothermal gradient by the second step, to search for the model that provides the best fit
414 to both the age data and the modern geothermal gradient. This study uses the following compound
415 misfit function to evaluate the models:

$$\Phi = \Phi_{\tau} + \Phi_{\gamma}/\sqrt{N}, \quad (17)$$

416 where Φ_{τ} and Φ_{γ} are misfit values for the age and geothermal gradient calculated using the
417 equations 12 and 13, and N is the number of age inputs. Dividing Φ_{γ} by the square root of N in this
418 equation, as also done for calculating the Φ_{τ} (equation 12), means that the modern geothermal
419 gradient is given the same weight as an age input for evaluating the model.
420
421

422 **8. Synthetic models for testing the new modeling guideline**

423 We firstly test our stepwise inversion scheme by synthetic datasets generated by thermo-
424 kinematic models modified from Braun et al. (2012) (their Fig. 9). The synthetic age dataset is
425 produced by *Pecube* using the following parameters: a steady-state topography with a 20-km
426 wavelength and a 2-km relief, a model block thickness of 30 km with a basal temperature of 600 °C,
427 a thermal diffusivity of 25 km²/Myr, a sea level temperature of 10 °C, a lapse rate of 5 °C/km.
428 Worth noting is that these parameters are the same as Braun et al. (2012). For model details, see
429 Braun et al. (2012). For model setup see the supplementary Figure S1.

430 Synthetic AFT and AHe ages (supplementary Tables T1) were calculated for both surface
431 and borehole samples for four different exhumation histories. The synthetic models a and b are
432 characterized by a sudden decrease in exhumation rate from 1 km/Myr to 0.1 km/Myr (model-a,
433 same as the that shown in the Fig. 9 of Braun et al. 2012) and 0.3 km/Myr (model-b) at 5 Ma,
434 respectively. The models c and d include a sudden increase in exhumation rate from 0.3 km/Myr

Deleted: 20

Deleted: 150

437 (model-c) and 0.1 km/Myr (model-d) to 1 km/Myr at 5 Ma, respectively. All models start from 40
438 Ma. Except for the synthetic age data (plotted in the first row of Fig. 9), these four models generate
439 modern geothermal gradients of 26.5 °C/km, 28.6 °C/km, 35.5 °C/km and 34 °C/km for the
440 uppermost 2-km crust, respectively.

441 Inversion of rock exhumation history used a start time of 20 Ma and a time interval length
442 of 1.0 Myr for all synthetic datasets, which were assigned with a 6% uncertainty. As shown by the
443 modelling output visualized in Fig. 9a, our inversion of the rock exhumation from the synthetic
444 dataset-a finds an optimal initial geothermal gradient of 22 °C/km and *a priori* rate of 0.85 ± 0.25
445 km/Myr, and yields a decrease in exhumation rates from ~0.9 km/Myr (before 6 Ma) to 0.3-0.1
446 km/Myr (4-0 Ma), via a gradual decrease during 6-4 Ma. The data has no resolution for the
447 exhumation history before 10 Ma. Comparing to the synthetic model (abrupt decrease from 1
448 km/Myr to 0.1 km/Myr at 5 Ma), the rates before 5 Ma are underestimated by 0.1 km/Myr, whereas
449 the values after 5 Ma overestimated by 0.1-0.3 km/Myr.

450 The inversion for the synthetic dataset-b results in an optimal initial geothermal gradient
451 of 21.7 °C/km and *a priori* rate of 0.81 ± 0.24 km/Myr, and an increase in exhumation rates from
452 ~0.85 (before 5 Ma) km/Myr to 0.4-0.5 km/Myr (4-0 Ma), via a gradual decrease during 5-4 Ma
453 (Fig. 9b). Comparing to the synthetic model (abrupt decrease from 1 km/Myr to 0.3 km/Myr at 5
454 Ma), the rates before 5 Ma are underestimated, whereas the values before 5 Ma are overestimated
455 by ~0.1-0.2 km/Myr.

456 The inversion for the synthetic dataset-c yields an optimal initial geothermal gradient of
457 24.3 °C/km and *a priori* rate of 0.55 ± 0.17 km/Myr, and a decrease in exhumation rates from
458 ~0.45-0.3 km/Myr (before 5 Ma) to 1.0 km/Myr (3-0 Ma), via a gradual increase during 5-3 Ma
459 (Fig. 9c). Comparing to the synthetic model (abrupt decrease from 0.3 km/Myr to 1.0 km/Myr at

Formatted: Font: Italic

460 5 Ma), the rates during 5-3 Ma are underestimated, whereas the rates before 5 Ma overestimated
461 by 0-0.15 km/Myr.

462 The inversion for the synthetic dataset-d produces an optimal initial geothermal gradient
463 of 24.5 °C/km and a priori rate of 0.25 ± 0.08 km/Myr, and an increase in exhumation rates from
464 ~0.1-0.2 km/Myr (before 5 Ma) to 1.0 km/Myr (3-0 Ma), via a gradual decrease during 5-3 Ma
465 (Fig. 9d). Comparing to the synthetic model (abrupt decrease from 1 km/Myr to 0.3 km/Myr at 5
466 Ma), the rates before 5 Ma are slightly overestimated, whereas the values during 5-3 Ma are
467 underestimated.

468 To summarize, the inverted rock exhumation histories for the four synthetic datasets match
469 the whole picture of the synthetic “truth”, but the variations in exhumation are underestimated,
470 and the sharp changes at 5 Ma are smoothed. It is worth noting that inversions using only surface
471 samples produce similar results (supplementary Fig. S2).

473 **9. Natural examples for testing the new modeling guideline**

474 Below we use three examples to demonstrate our new method. The Denali data is used
475 again for demonstrating the efficiency of our method in finding the proper initial geothermal
476 gradient and the a priori exhumation rate. Then, we further test our method using the Himalayan
477 Dhanladar range and KTB borehole (the Continental Deep Drilling Project in Germany)
478 thermochronologic data for representing regions of fast and slow erosion, respectively.

479 **9.1 The Denali transect**

480 Using the stepwise inversion modeling guideline, the Denali transect yields an exhumation
481 history generally similar with that of the reference model (Fig. 10a). Differences in the *a priori*
482 parameters include that the new inversion finds and uses an initial geothermal gradient of

Deleted: 8

Deleted: Examples

Formatted: Font: Italic

Deleted: 8

Deleted: strategy

487 25.2 °C/km (slightly higher than that of the reference model), *a priori* erosion rate of 0.46 ± 0.23
488 km/Myr (slightly lower than that of the reference model) and a time interval length of 1.5 Ma. The
489 combination of these *a priori* parameters result in a major increase in erosion rate, to 0.55-0.6
490 km/Myr at 6 Ma, which is 1.5 Myr latter than that of the reference model (7.5 Ma). The subtle
491 differences from the reference model mainly result from the time interval length used in these
492 models. Comparing the misfit values, the new model produces slightly better fits than the reference
493 model, with the *a posterior* misfit values of 1.81 and 0.11 for the observed age and geothermal
494 data.

495

496 9.2 Himalayan Dharladar range transect

497 AFT and ZHe data from the Dharladar range in the northwestern Himalayas, reported in
498 the publications by Deeken et al. (2011) and Thiede et al. (2017) are used as an example for regions
499 of young cooling ages and fast exhumation. The samples were collected in an elevation range
500 between 1.5 and 4.5 km, covering a topographic relief of 3 km within a spatial distance of ~15 km
501 on the hanging wall of the main central thrust of the Himalayan fold-thrust-belt (Deeken et al.,
502 2011; Thiede et al., 2017). AER slope regression of ZHe and AFT ages performed in Deeken et al.
503 (2011) produced apparent erosion rates of ~2.8 km/Myr and ~0.2 km/Myr for the time intervals
504 6.4–14.5 Ma and 1.7–3.7 Ma, respectively, implying a potential increase in erosion rates at ~3.7-
505 6.4 Ma. Using geothermal gradients of 25-45 °C/km, time-averaged erosion rates were estimated
506 as 0.8-2.0 km/Myr since 3.7 Ma (Deeken et al., 2011).

507 The modelling of the Dharladar range data uses a modern geothermal gradient constraint
508 of 45 ± 8 °C/km (Deeken et al., 2011). The relatively large uncertainty is assigned for the
509 geothermal gradient, because of the absence of direct geothermal measurements in the study area.

Deleted: 4.

Deleted: 7

Deleted: 3

Deleted: 6

Deleted: 1

Deleted: 8

Deleted: s

Deleted: of

Deleted: 6

Deleted: 70

Deleted: since

Deleted: slightly

Deleted: different

Deleted: 6

Deleted: 6

Deleted: 0

Deleted:)

Deleted: (Fig. 9a)

Deleted: 8

Deleted: central

Deleted: AER slope regression suggests an increase in apparent erosion rates from ~0.2 km/Myr to ~2.8 km/Myr at ~3.7-6.4 Ma

Deleted: and 0.8-1.7 km/My

Deleted: and 14.5 Ma, respectively

535 Our exhumation inversion for the AER data using the stepwise modeling guideline yields relatively
536 slow rates of 0.1-0.6 km/Myr and fast rates of 1.2-1.6 km/Myr before and after ~3 Ma, respectively
537 (Fig. 10b). The abrupt increase of exhumation rates at ~3 Ma is generally consistent with the
538 estimates from the slope regression results of Deeken et al. (2011). However, the inverted
539 exhumation rates since 3 Ma are significantly lower than the estimation from the AER slope (~2.8
540 km/Myr), which is likely due to the overestimation of exhumation of the AER slope due to
541 topographic perturbation of isotherms. Such a perturbation is a function of exhumation rates: the
542 higher the exhumation, the larger the perturbation (Glotzbach et al., 2015). The modelling yields
543 a history of the geothermal gradient that gradually increases to a modern value of ~46 °C/km, close
544 to the input value (45 ± 8 °C/km).

Deleted: strategy

Deleted: 2

Deleted: 4

Deleted: relatively

Deleted: 3

Deleted: 5

Deleted: 6-5

Deleted: 9b

Deleted: 6-

Deleted: 5

Deleted: 44

545

546 2.3 KTB borehole

Deleted: 8

547 The KTB borehole yields a large thermochronologic and geochronologic age data
548 (Warnock and Zeitler, 1998; Stockli and Farley, 2004). Previous studies suggest the borehole are
549 truncated by multiple faults, which offset the age-depth relationship (Wagner et al., 1997). Here
550 we use the data at depths shallower than 1 km, where data are abundant and have linear relationship
551 with depths.

552 The KTB apatite, zircon and titanite (U-Th)/He (AHe, ZHe and THe) and AFT age data
553 vary largely between 85-50 Ma. These clustered ages have been interpreted as indicating a late
554 Cretaceous phase of exhumation, followed by slow exhumation (Wagner et al., 1997; Stockli and
555 Farley, 2004), as also shown by previous thermal history reconstructions based on k-feldspar
556 $^{40}\text{Ar}/^{39}\text{Ar}$ data (Warnock and Zeitler, 1998).

569 Our modeling, using the AER data and a modern geothermal gradient of 27.5 ± 2.8 °C/km
570 (Clauser et al., 1997), shows that elevated exhumation rates (0.1-0.13 km/Myr) between 80-50 Ma,
571 followed by slower exhumation rates of ~0.04 km/Myr (Fig. 10c), are similar to previous estimates
572 (Wagner et al., 1997; Warnock and Zeitler, 1998; Stockli and Farley, 2004). Associated with
573 changes in exhumation, geothermal gradient gradually decreases from the peak values at 70-60
574 Ma to a value of ~28 °C/km at the present-day.

Deleted: 2

Deleted: 15

Deleted: 60

Deleted: 9c

575

576 **10. Conclusion**

Deleted: 9

577 The *a priori* information has important effects on the inversion results using the least-
578 squares inversion method. Our study demonstrates the importance of geothermal gradient and the
579 *a priori* exhumation rate in estimating the exhumation history from the thermochronology data.

580 To take into account the geothermal data into the exhumation history inversion, we outlined a
581 stepwise inversion method that first searches for the appropriate initial geothermal gradient, which
582 is then used in the modelling searching for the *a priori* exhumation rate. Our modelling guideline
583 produces exhumation history and geothermal gradient that provide reasonable fits for both the
584 observed AER and modern geothermal data, as tested by datasets of both synthetic models and
585 natural samples. The code and data used in this work are available in GITHUB
586 (https://github.com/yuntao-github/A2E_app).

Deleted: propose

Deleted: model

Deleted: strategy

Deleted: will

Deleted: be

Deleted: Our

Deleted: strategy

587

588 **Code availability**

589 The code used in this work are available in GITHUB (https://github.com/yuntao-github/A2E_app).

590

591 **Data availability**

604 The data used in this work are available in GITHUB (https://github.com/yuntao-github/A2E_app).

Deleted: <https://github.com/yuntao-github/code4modelAER>

605

606 **Author contribution**

607 Yuntao Tian: Conceptualization, Methodology, Software, Data curation, Visualization,
608 Investigation, Writing- Original draft preparation. Lili Pan: Visualization, Writing- Reviewing and
609 Editing. Guihong Zhang and Xinbo Yao: Writing- Reviewing and Editing.

610

611 **Competing interests**

612 The contact author has declared that none of the authors has any competing interests.

613

614 **Acknowledgments**

615 This study is funded by the National Natural Science Foundation of China (42172229, 41888101
616 and 41772211). Discussions with Jie Hu and Donglan Zeng are gratefully appreciated. [Comments](#)
617 [and suggestions from Gilby Jepson and Christoph Glotzbach clarified many points of this work.](#)

618

619 **References:**

620 Anderson, J. L., Barth, A. P., Wooden, J. L., and Mazdab, F.: Thermometers and
621 Thermobarometers in Granitic Systems, *Rev. Mineral. Geochem.*, 69, 121-142,
622 10.2138/rmg.2008.69.4, 2008.

623 Armstrong, P. A.: Thermochronometers in Sedimentary Basins, *Rev. Mineral. Geochem.*, 58,
624 499-525, 10.2138/rmg.2005.58.19, 2005.

625 Ault, A. K., Gautheron, C., and King, G. E.: Innovations in (U–Th)/He, Fission Track, and
626 Trapped Charge Thermochronometry with Applications to Earthquakes, Weathering, Surface-
627 Mantle Connections, and the Growth and Decay of Mountains, *Tectonics*, 38, 3705-3739,
628 10.1029/2018TC005312, 2019.

630 Batt, G. E. and Brandon, M. T.: Lateral thinking: 2-D interpretation of thermochronology in
631 convergent orogenic settings, *Tectonophysics*, 349, 185-201, 2002.

632 Brandon, M. T., Roden-Tice, M. K., and Garver, J. I.: Late Cenozoic exhumation of the Cascadia
633 accretionary wedge in the Olympic Mountains, Northwest Washington State, *Bull. Geol. Soc.
634 Am.*, 110, 985-1009, 1998.

635 Braun, J.: Quantifying the effect of recent relief changes on age-elevation relationships, *Earth
636 Planet. Sci. Lett.*, 200, 331-343, 2002.

637 Braun, J.: Pecube: a new finite-element code to solve the 3D heat transport equation including
638 the effects of a time-varying, finite amplitude surface topography, *Comput. Geosci.*, 29, 787-794,
639 2003.

640 Braun, J., van der Beek, P., Valla, P., Robert, X., Herman, F., Glotzbach, C., Pedersen, V., Perry,
641 C., Simon-Labric, T., and Prigent, C.: Quantifying rates of landscape evolution and tectonic
642 processes by thermochronology and numerical modeling of crustal heat transport using
643 PECUBE, *Tectonophysics*, 524-525, 1-28, 10.1016/j.tecto.2011.12.035, 2012.

644 Burbank, D. W., Blythe, A. E., Putkonen, J., Pratt-Sitaula, B., Gabet, E., Oskin, M., Barros, A.,
645 and Ojha, T. P.: Decoupling of erosion and precipitation in the Himalayas, *Nature*, 426, 652-655,
646 2003.

647 Clauser, C., Giese, P., Huenges, E., Kohl, T., Lehmann, H., Rybach, L., Šafanda, J., Wilhelm,
648 H., Windloff, K., and Zoth, G.: The thermal regime of the crystalline continental crust:
649 Implications from the KTb, *J Geophys Res: Solid Earth*, 102, 18417-18441,
650 <https://doi.org/10.1029/96JB03443>, 1997.

651 Deeken, A., Thiede, R. C., Sobel, E. R., Hourigan, J. K., and Strecker, M. R.: Exhumational
652 variability within the Himalaya of northwest India, *Earth Planet. Sci. Lett.*, 305, 103-114,
653 10.1016/j.epsl.2011.02.045, 2011.

654 Dodson, M. H.: Closure temperature in cooling geochronological and petrological systems,
655 *Contrib. Mineral. Petrol.*, 40, 259-274, 1973.

656 Ehlers, T. A.: Crustal Thermal Processes and the Interpretation of Thermochronometer Data,
657 Rev. Mineral. Geochem., 58, 315-350, 10.2138/rmg.2005.58.12, 2005.

658 Ehlers, T. A. and Farley, K. A.: Apatite (U-Th)/He thermochronometry: methods and
659 applications to problems in tectonic and surface processes, Earth Planet. Sci. Lett., 206, 1-14,
660 2003.

661 Fitzgerald, P. G., Sandiford, M., Barrett, P. J., and Gleadow, A. J. W.: Asymmetric extension
662 associated with uplift and subsidence in the Transantarctic Mountains and Ross Embayment,
663 Earth Planet. Sci. Lett., 81, 67-78, [http://dx.doi.org/10.1016/0012-821X\(86\)90101-9](http://dx.doi.org/10.1016/0012-821X(86)90101-9), 1986.

664 Fitzgerald, P. G., Sorkhabi, R. B., Redfield, T. F., and Stump, E.: Uplift and denudation of the
665 central Alaska Range: A case study in the use of apatite fission track thermochronology to
666 determine absolute uplift parameters, J Geophy Res: Solid Earth, 100, 20175-20191,
667 doi:10.1029/95JB02150, 1995.

668 Fox, M., Herman, F., Kissling, E., and Willett, S. D.: Rapid exhumation in the Western Alps
669 driven by slab detachment and glacial erosion, Geology, 43, 379-382, 2015.

670 Fox, M., Herman, F., Willett, S. D., and May, D. A.: A linear inversion method to infer
671 exhumation rates in space and time from thermochronometric data, Earth Surf. Dynam., 2, 47-
672 65, 10.5194/esurf-2-47-2014, 2014.

673 Gallagher, K.: Transdimensional inverse thermal history modelling for quantitative
674 thermochronology, J. Geophys. Res., 117, B02408, doi:10.1029/2011JB008825., 2012.

675 Glotzbach, C., Braun, J., and van der Beek, P.: A Fourier approach for estimating and correcting
676 the topographic perturbation of low-temperature thermochronological data, Tectonophysics, 649,
677 115-129, <https://doi.org/10.1016/j.tecto.2015.03.005>, 2015.

678 Herman, F., Seward, D., Valla, P. G., Carter, A., Kohn, B., Willett, S. D., and Ehlers, T. A.:
679 Worldwide acceleration of mountain erosion under a cooling climate, Nature, 504, 423-426,
680 2013.

681 House, M. A., Wernicke, B. P., and Farley, K. A.: Paleo-geomorphology of the Sierra Nevada,
682 California, from (U-Th)/He ages in apatite, *Am. J. Sci.*, 301, 77-102, 2001.

683 Hu, S. B., Raza, A., Min, K., Kohn, B. P., Reiners, P. W., Ketcham, R. A., Wang, J. Y., and
684 Gleadow, A. J. W.: Late Mesozoic and Cenozoic thermotectonic evolution along a transect from
685 the north China craton through the Qinling orogen into the Yangtze craton, central China,
686 *Tectonics*, 25, 10.1029/2006TC001985., 2006.

687 Jiao, R., Herman, F., and Seward, D.: Late Cenozoic exhumation model of New Zealand:
688 Impacts from tectonics and climate, *Earth-Science Reviews*, 166, 286-298,
689 <https://doi.org/10.1016/j.earscirev.2017.01.003>, 2017.

690 Ketcham, R. A.: Forward and Inverse Modeling of Low-Temperature Thermochronometry Data,
691 *Rev. Mineral. Geochem.*, 58, 275-314, 10.2138/rmg.2005.58.11, 2005.

692 Laslett, G., Green, P. F., Duddy, I., and Gleadow, A.: Thermal annealing of fission tracks in
693 apatite 2. A quantitative analysis, *Chem. Geol.*, 65, 1-13, 1987.

694 Mancktelow, N. S. and Grasemann, B.: Time-dependent effects of heat advection and
695 topography on cooling histories during erosion, *Tectonophysics*, 270, 167-195,
696 [https://doi.org/10.1016/S0040-1951\(96\)00279-X](https://doi.org/10.1016/S0040-1951(96)00279-X), 1997.

697 McInnes, B. I. A., Evans, N. J., Fu, F. Q., and Garwin, S.: Application of Thermochronology to
698 Hydrothermal Ore Deposits, *Rev. Mineral. Geochem.*, 58, 467-498, 10.2138/rmg.2005.58.18,
699 2005.

700 Reiners, P. W. and Brandon, M. T.: Using thermochronology to understand orogenic erosion,
701 *Ann Rev Earth Planet Sci*, 34, 419-466, 2006.

702 Schildgen, T. F., van der Beek, P. A., Sinclair, H. D., and Thiede, R. C.: Spatial correlation bias
703 in late-Cenozoic erosion histories derived from thermochronology, *Nature*, 559, 89-93,
704 10.1038/s41586-018-0260-6, 2018.

705 Stalder, N. F., Herman, F., Fellin, M. G., Coutand, I., Aguilar, G., Reiners, P. W., and Fox, M.:
706 The relationships between tectonics, climate and exhumation in the Central Andes (18–36°S):

707 Evidence from low-temperature thermochronology, *Earth-Science Reviews*, 210, 103276,
708 <https://doi.org/10.1016/j.earscirev.2020.103276>, 2020.

709 Stockli, D. F. and Farley, K. A.: Empirical constraints on the titanite (U–Th)/He partial retention
710 zone from the KTB drill hole, *Chem. Geol.*, 207, 223-236,
711 <https://doi.org/10.1016/j.chemgeo.2004.03.002>, 2004.

712 Sutherland, R., Gurnis, M., Kamp, P. J. J., and House, M. A.: Regional exhumation history of
713 brittle crust during subduction initiation, Fiordland, southwest New Zealand, and implications for
714 thermochronologic sampling and analysis strategies, *Geosphere*, 5, 409-425,
715 10.1130/GES00225.1, 2009.

716 Tarantola, A.: *Inverse Problem Theory and Methods for Model Parameter Estimation*, SIAM,
717 Philadelphia2005.

718 Thiede, R., Robert, X., Stübner, K., Dey, S., and Faruhn, J.: Sustained out-of-sequence
719 shortening along a tectonically active segment of the Main Boundary thrust: The Dhauladhar
720 Range in the northwestern Himalaya, *Lithosphere*, 9, 715-725, 10.1130/L630.1, 2017.

721 Tian, Y., Kohn, B. P., Hu, S., and Gleadow, A. J. W.: Synchronous fluvial response to surface
722 uplift in the eastern Tibetan Plateau: Implications for crustal dynamics, *Geophys. Res. Lett.*, 42,
723 29-35, 10.1002/2014GL062383, 2015.

724 Turcotte, D. and Schubert, G.: *Geodynamics*, Cambridge University Press2002.

725 Valla, P. G., van der Beek, P. A., and Braun, J.: Rethinking low-temperature thermochronology
726 data sampling strategies for quantification of denudation and relief histories: A case study in the
727 French western Alps, *Earth Planet. Sci. Lett.*, 307, 309-322, 10.1016/j.epsl.2011.05.003, 2011.

728 van der Beek, P. and Schildgen, T. F.: Short communication: age2exhume – a MATLAB/Python
729 script to calculate steady-state vertical exhumation rates from thermochronometric ages and
730 application to the Himalaya, *Geochronology*, 5, 35-49, 10.5194/gchron-5-35-2023, 2023.

731 van der Beek, P. A., Valla, P. G., Herman, F., Braun, J., Persano, C., Dobson, K. J., and Labrin,
732 E.: Inversion of thermochronological age-elevation profiles to extract independent estimates of

733 denudation and relief history -- II: Application to the French Western Alps, *Earth Planet. Sci.*
734 *Lett.*, 296, 9-22, DOI: 10.1016/j.epsl.2010.04.032, 2010.

735 Vermeesch, P.: IsoplotR: A free and open toolbox for geochronology, *Geoscience Frontiers*, 9,
736 1479-1493, <https://doi.org/10.1016/j.gsf.2018.04.001>, 2018.

737 Wagner, G. A., Coyle, D. A., Duyster, J., Henjes-Kunst, F., Peterek, A., Schröder, B., Stöckhert,
738 B., Wemmer, K., Zulauf, G., Ahrendt, H., Bischoff, R., Hejl, E., Jacobs, J., Menzel, D., Lal, N.,
739 Van den haute, P., Vercoutere, C., and Welzel, B.: Post-Variscan thermal and tectonic evolution
740 of the KTB site and its surroundings, *J Geophys Res: Solid Earth*, 102, 18221-18232,
741 <https://doi.org/10.1029/96JB02565>, 1997.

742 Warnock, A. C. and Zeitler, P. K.: $^{40}\text{Ar}/^{39}\text{Ar}$ thermochronometry of K-feldspar from the KTB
743 borehole, Germany, *Earth Planet. Sci. Lett.*, 158, 67-79, [https://doi.org/10.1016/S0012-](https://doi.org/10.1016/S0012-821X(98)00044-2)
744 [821X\(98\)00044-2](https://doi.org/10.1016/S0012-821X(98)00044-2), 1998.

745 Whipp Jr., D. M., Ehlers, T. A., Blythe, A. E., Huntington, K. W., Hodges, K. V., and Burbank,
746 D. W.: Plio-Quaternary exhumation history of the central Nepalese Himalaya: 2.
747 Thermokinematic and thermochronometer age prediction model, *Tectonics*, 26,
748 10.1029/2006tc001991, 2007.

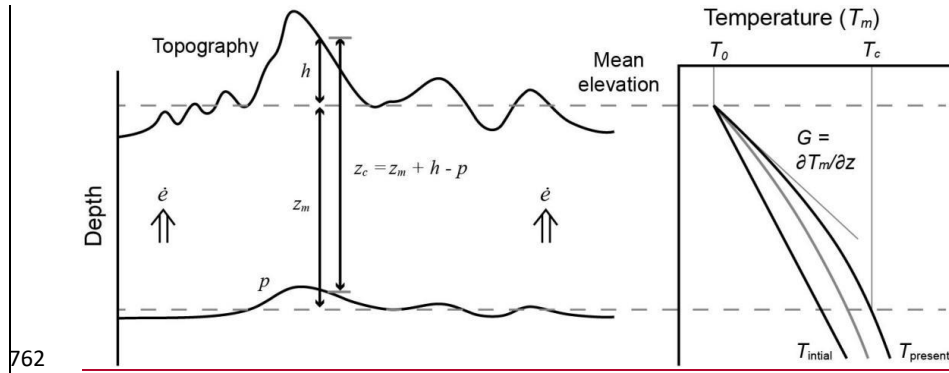
749 Willett, S. D. and Brandon, M. T.: Some analytical methods for converting thermochronometric
750 age to erosion rate, *Geochem. Geophys. Geosyst.*, 14, 209-222, 10.1029/2012gc004279, 2013.

751 Willett, S. D., Herman, F., Fox, M., Stalder, N., Ehlers, T. A., Jiao, R., and Yang, R.: Bias and
752 error in modelling thermochronometric data: resolving a potential increase in Plio-Pleistocene
753 erosion rate, *Earth Surf. Dynam. Discuss.*, 2020, 1-78, 10.5194/esurf-2020-59, 2020.

754 Zeitler, P., Meltzer, A., Koons, P., Craw, D., Hallet, B., Chamberlain, C., Kidd, W., Park, S.,
755 Seeber, L., Bishop, M., and Shroder, J. F.: Erosion, Himalayan Geodynamics, and the
756 Geomorphology of Metamorphism, *GSA Today*, 11, 4-9, 10.1130/1052-
757 5173(2001)011<0004:EHGATG>2.0.CO;2, 2001.

758
759
760

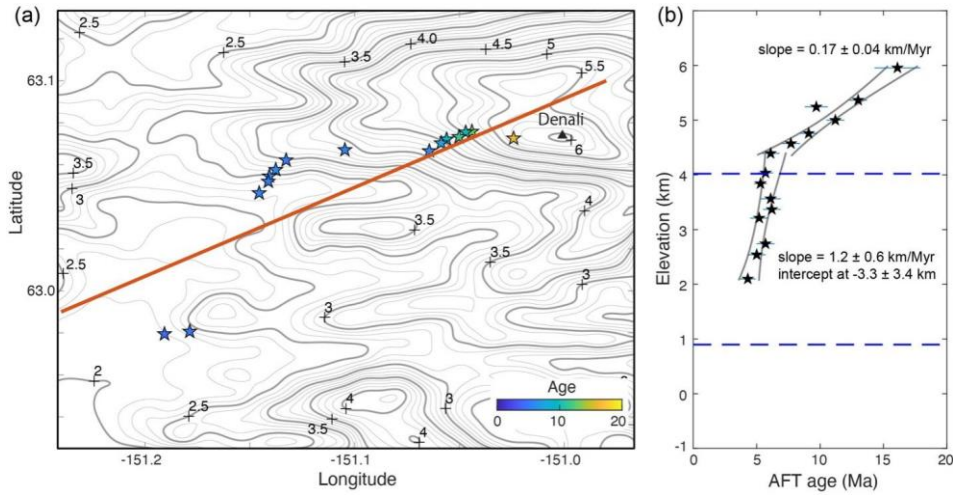
761 **Figures captions:**



763 Figure 1. Schematics showing the relationship among closure depth (z_c), topography and its
764 perturbation (p). The parameter h denotes the difference between the sample and the mean
765 elevation, and z_m the depth of the closure temperature (T_c , the lower dashed line) derived from
766 the mean elevation (upper dashed line) and initial temperature field ($T_{initial}$) and exhumation
767 history (\dot{e}).

768

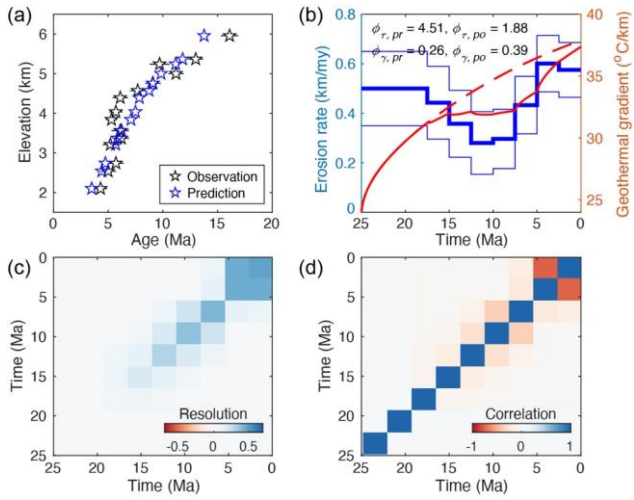
769



770

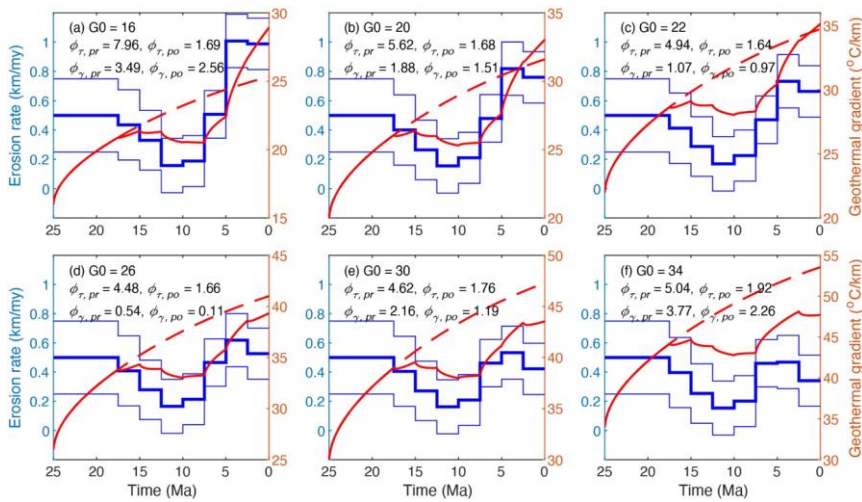
771 Figure 2. (a) Distribution of AFT age data (pentagons, colored by age values) over the elevation
772 contour map computed using the SRTM30 data of the Denali massif in Alaska. AFT data
773 sourced from Fitzgerald et al. (1995). (b) AER and the slope fitting results using isoplotR
774 (Vermeesch, 2018). AER fitting of ages older than 6.7 Ma yields a slope of 0.17 ± 0.04 km/Myr;
775 whereas the fitting of ages between 6.5 Ma and 4.3 Ma produces a slope of 1.2 ± 0.6 km/Myr
776 and an intercept at -3.3 ± 3.4 km. The upper and lower dashed lines denote the mean elevation
777 (4.02 km) and the depth of the nominal closure temperature (110 °C), calculated using the
778 modern geothermal gradient (38.9 °C/km) and the surface temperature (-12 °C).

779

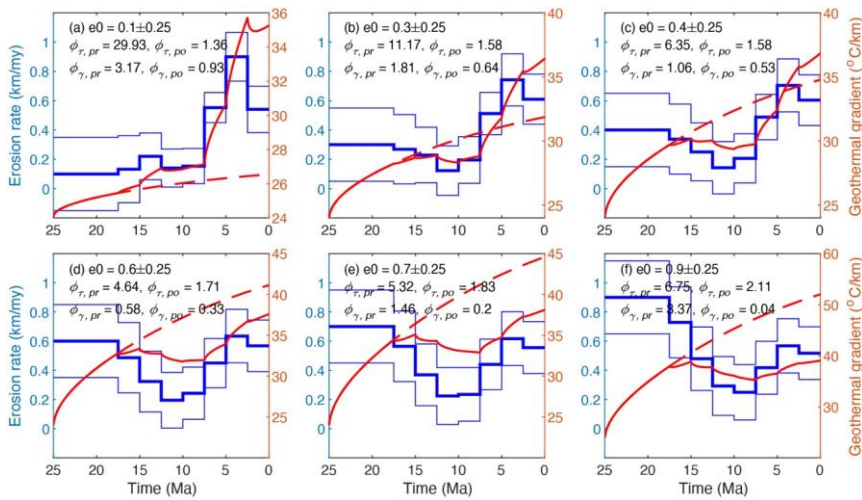


780

781 Figure 3. Inputs and outputs of the reference model for the Denali AFT. (a) Comparison between
 782 the observed (in black) and predicted (in blue) AER. (b) The *a posteriori* exhumation history
 783 generated by the reference model. Thick and thin lines are the mean and one standard deviation
 784 of the inverted exhumation history. The red dash and solid lines are the history of the geothermal
 785 gradients, predicted by the *a priori* and *a posteriori* models, respectively. (c) and (d) Plots of the
 786 resolution and correlation matrix.

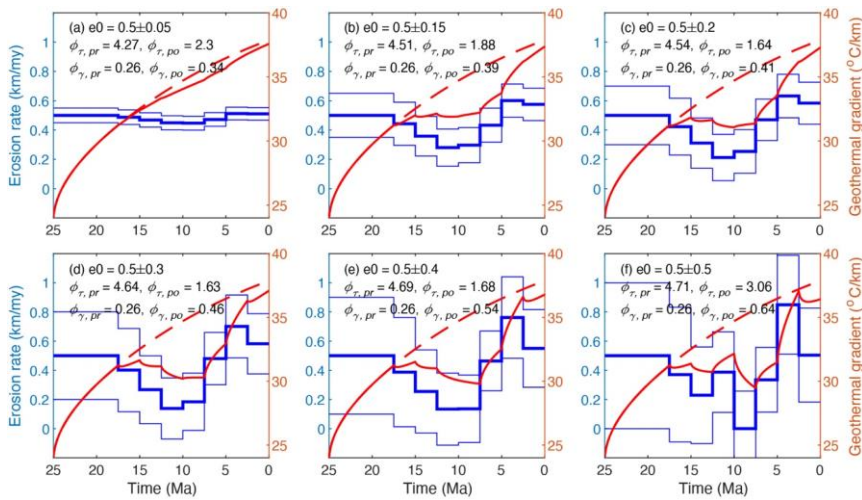


787
 788 Figure 4. Histories of exhumation and geothermal gradients, predicted by models using different
 789 initial geothermal gradients between 18 °C/km and 34 °C/km. The blue thick and thin lines are
 790 the mean and one standard deviation of the inverted exhumation history. The red dash and solid
 791 lines are the history of the geothermal gradients, predicted by the *a priori* and *a posteriori*
 792 models, respectively. Except for the initial geothermal gradient, other parameters are the same as
 793 the reference model. Comparing to the reference model which used an initial geothermal gradient
 794 of 24 °C/km (Fig. 3), models using a lower initial geothermal gradient yield relatively higher
 795 exhumation rates (panels a-c), whereas those using a higher gradient produce lower exhumation
 796 rates (panels d-f).



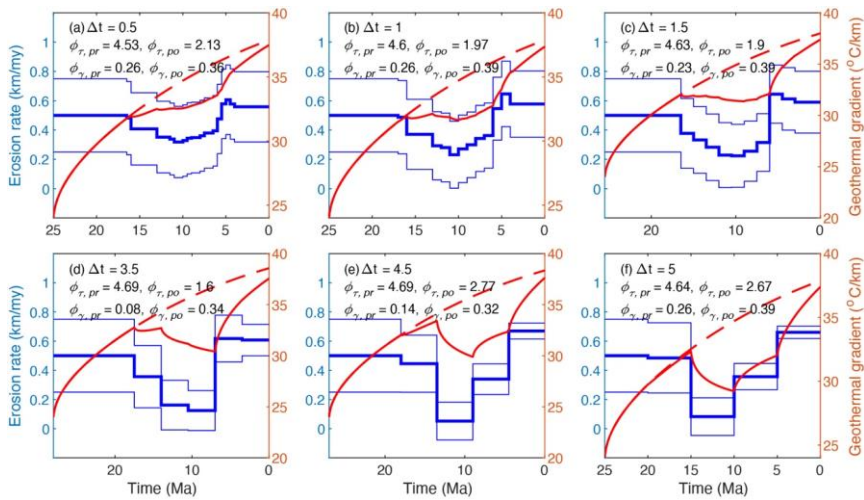
798
 799 Figure 5. Histories of exhumation and geothermal gradients, predicted by models using different
 800 *a priori* mean values of the exhumation rates, ranging from 0.1 km/Myr to 0.9 km/Myr. Other
 801 parameters are the same as the reference model. For explanation of the plotted lines, see Figure
 802 4. Comparing to the reference model which used *a priori* mean exhumation of 0.5 km/Myr (Fig.
 803 3), models using a lower *a priori* exhumation yield relatively higher exhumation rates for the last
 804 three stages (7.5 - 0 Ma) (panels a-c), whereas those using a higher *a priori* exhumation produce
 805 lower exhumation rates for the last three stages (panels d-f).

806



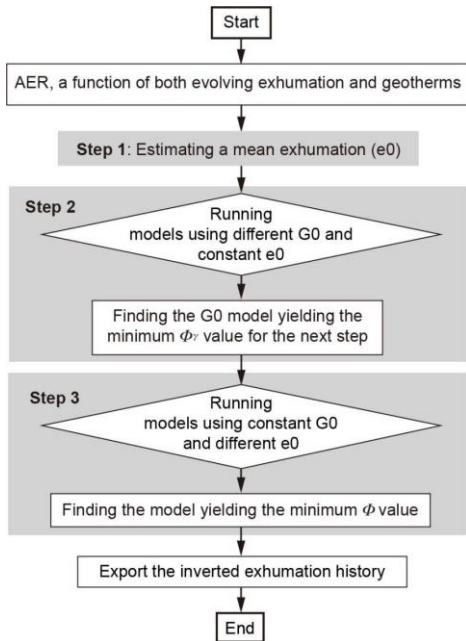
807
 808 Figure 6. Histories of exhumation and geothermal gradients, predicted by models using different
 809 *a priori* variance values (between 0.05 km/Myr and 0.5 km/Myr) of the exhumation rates (0.5
 810 km/ Myr). Other parameters are the same as the reference model. For explanation of the plotted
 811 lines, see Figure 4. Comparing to the reference model which used *a priori* variance of the
 812 exhumation (0.25 km/Myr) (Fig. 3), models using a lower *a priori* variance yield limited
 813 variations and uncertainties in exhumation (panels a-c), whereas those using a higher *a priori*
 814 variance produce larger variations and uncertainties (panels d-f).

815



816
 817 Figure 7. Histories of exhumation and geothermal gradients, predicted by models using different
 818 time interval lengths. Other parameters are the same as the reference model. For explanation of
 819 the plotted lines, see Figure 4. Comparing to the reference model which used a time interval
 820 length of 2.5 Ma (Fig. 3), models using smaller time interval lengths yield lower variations in
 821 exhumation (panels a-c) than other using larger time interval lengths (panels d-f).

822



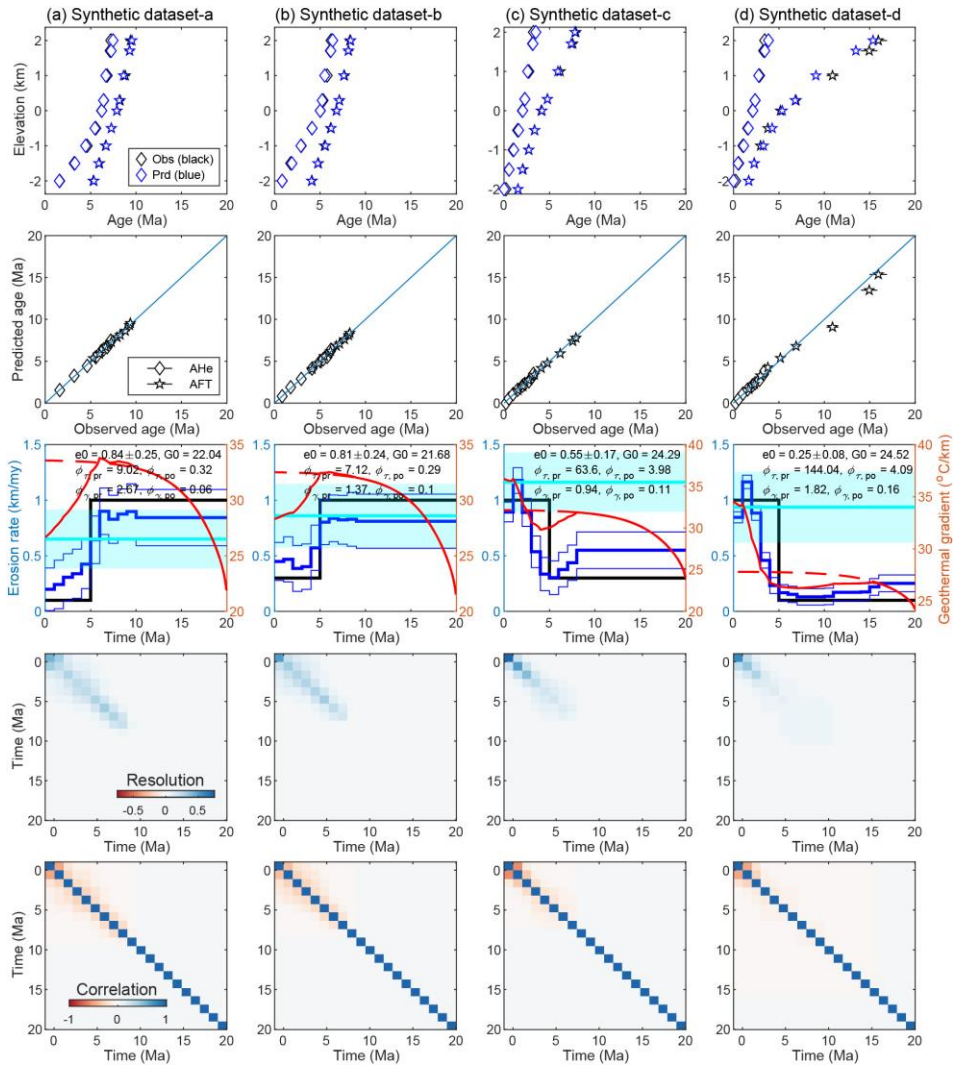
823

824 Figure 8. Flow chat of a stepwise modeling method, which includes three main steps. The first
 825 step estimates a mean exhumation rate (e_0) using the nominal closure temperatures, modern
 826 geothermal gradient and sample ages. The mean rate is used in the second step which runs a set
 827 of models using different initial geothermal gradients for optimizing the initial geothermal
 828 model. The third step runs a set of models using different *a priori* exhumation rates, which is
 829 generated around the mean rate, and the optimized initial geothermal model by the second step,
 830 to find the best model that yields the minimum misfit to both age data and modern geothermal
 831 gradient.

832

Deleted: the proposed

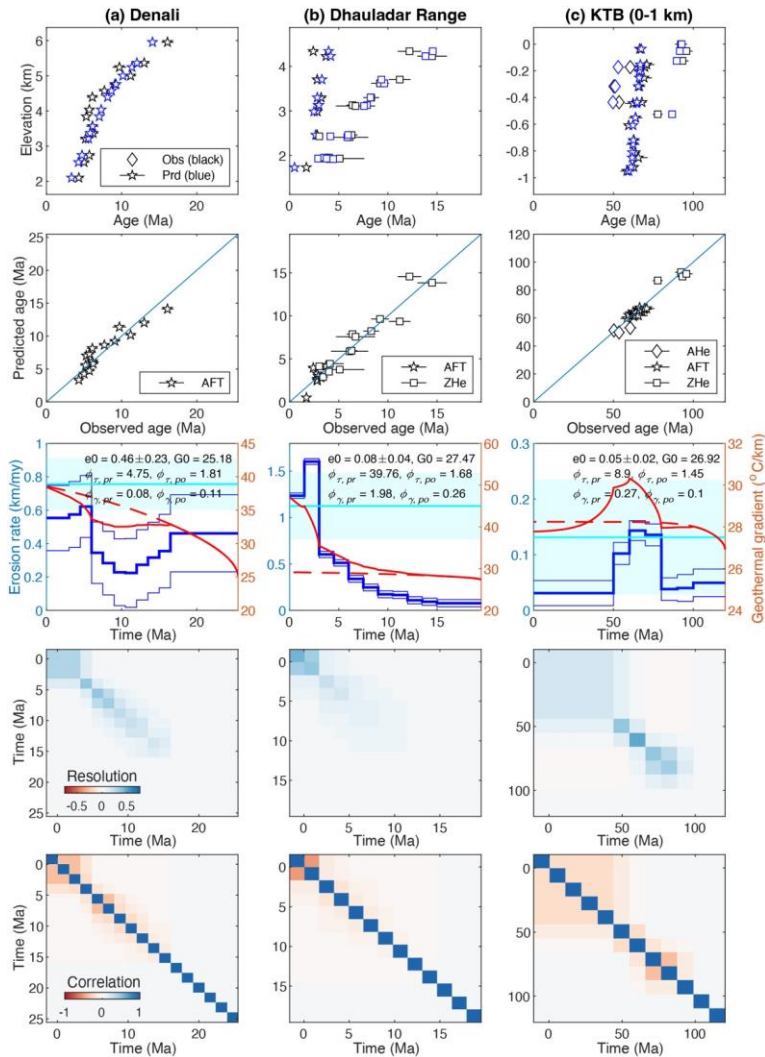
Deleted: strategy



835
 836 Figure 9. The best-fit model for the synthetic dataset-a, -b, -c and -d using the modeling method
 837 shown in figure 8. First row: Comparison between the observed (in black) and predicted (in blue)
 838 AER. Second row: plots of observed and modeled ages. Third row: Histories of exhumation and
 839 geothermal gradients. The black line marks the “true” exhumation history used for simulating the

840 age dataset, whereas the blue thick and thin lines are the mean and one standard deviation of the
841 inverted exhumation. The red dash and solid lines are the history of the geothermal gradients,
842 predicted by the *a priori* and *a posterior* models, respectively, whereas the cyan line and polygon
843 denotes the modern geothermal gradient. Fourth and bottom row: Plots of the resolution and
844 correlation matrix.

845



846

847 Figure 10. The best-fit model for the Denali (a), Dhanladar range (b) and upper KTB (c)

848 transects, using the modeling method shown in figure 8. See Fig. 8 for panel interpretations.

Formatted: Left, Line spacing: Double

Deleted: 9

Deleted: strategy

Deleted: First row: Comparison between the observed (in black) and predicted (in blue) AER. Second row: plots of observed and modeled ages. Third row: Histories of exhumation and geothermal gradients. The blue thick and thin lines are the mean and one standard deviation of the inverted exhumation history. The red dash and solid lines are the history of the geothermal gradients, predicted by the *a priori* and *a posteriori* models, respectively. Fourth and bottom row: Plots of the resolution and correlation matrix.¶